Proceedings of the ASME 2016 Dynamic Systems and Control Conference
DSCC 2016
October 12-14, 2016, Minneapolis, USA

DSCC2016-9774

DYNAMICS OF A ROTOR-PENDULUM WITH A SMALL, STIFF PROPELLER IN WIND

William Craig, Derrick Yeo, and Derek A. Paley *
Department of Aerospace Engineering and
the Institute for Systems Research
University of Maryland
College Park, Maryland 20742
Email: wscraig@umd.edu, dyeo@umd.edu, dpaley@umd.edu

ABSTRACT

As small rotorcraft grow in capability, the possibilities for their application increase dramatically. Many of these new applications require stable outdoor flight, necessitating a closer look at the aerodynamic response of the aircraft in windy environments. This paper develops the equations of motion for a single-propeller test stand by analyzing the blade-flapping response of a small-stiff propeller in wind. The system dynamics are simulated to show behavior under various wind conditions, and stable system equilibria are identified. Experiments with a rotor-pendulum validate the simulations, including system equilibria and gust response.

INTRODUCTION

Small unmanned aerial systems (UAS) are transforming from hobbyist entertainment into utilitarian machines. UAS have been tasked with objectives such as surveying farmland and aiding in natural disasters [1] that require multi-rotor aircraft to fly outdoors in potentially adverse weather. High winds pose a great challenge to small UAS [2–4], and developing an understanding of how they respond to wind and the mechanics behind that response is key to compensating for them. This paper uses a combination of theoretical and experimental work to describe the forces and moments experienced by a single quadrotor-type propeller in a uniform wind. Experimental results are collected with a test stand in wind using a Gemfan 5030 propeller commonly used on quadrotor helicopters. These results promise to improve guidance and control algorithms for small, multi-rotor helicopters.

Although an important part of full-sized helicopter dynamics, blade-flapping is often assumed to be negligible in small quadrotor vehicles [5, 6]. For indoor flight with relatively small advance ratios, this assumption has proved valid even for highly aerobatic flight [7, 8]. However, for outdoor flight in wind, the effect of blade flapping and other aerodynamic phenomena must be re-evaluated [4]. When a helicopter rotor moves forward in air, the advancing side of the rotor produces more lift than the retreating side, which causes a roll moment on the blades [9]. Many studies [10–13] indicate that this moment causes the rotor blades to react with a maximum deflection at 90° phase delay, i.e., above the helicopter's nose, due either to a gyroscopic effect or the blade frequency response. Others provide the equations for flapping without explicitly indicating the expected phase delay [14, 15]. This paper provides a more comprehensive look at the blade-flap dynamics of a small, stiff propeller commonly used in small UAS.

Hoffmann et al. [12] and Yeo et al. [16] each measured a quadrotor propeller response to wind. Hoffmann et al. [12] tested a single propeller in wind to identify the flap angle, and showed that the hub experiences a force in the direction of the wind. Yeo et al. [16] tested a single-degree-of-freedom pitch stand with two propellers, as well as a fixed, rigid propeller in an edgewise flow, and found that forces and moments scale with free-stream velocity as suggested in [12].

This paper investigates the source of the forces and moments on a single propeller in wind, and describes blade-flapping dy-

*Address all correspondence to this author.

namics based on first-principle analyses. A simplified set of analytically tractable equations predict the phase delay and flap amplitude of a small, stiff propeller, the results of which are compared to experimental data. The experimental testbed consists of a two-degree-of-freedom rotor-pendulum, which is a spherical pendulum affixed with a spinning propeller. The long arm of the spherical pendulum increases the effect of the hub forces, demonstrating the propeller's response to wind.

The contributions of this paper are (1) a detailed analysis of the blade-flapping response of a small, stiff propeller in uniform wind, yielding the derivation and solution of the equations of motion for blade flapping and the rotor-pendulum system from first-principles; (2) comparison of the first-principles model to existing experimental measurements of forces and moments at the hub of a propeller fixed in a uniform wind; and (3) the design, fabrication, and testing of a rotor-pendulum test stand that demonstrates the effect of wind on a single propeller. This work increases the theoretical and physical understanding of a small, stiff propeller's response to wind, which has the potential to yield improved flight stability for small multi-rotor helicopters in adverse weather conditions by virtue of an improved feedback response using flow sensing and control [16].

The outline of the paper is as follows. The first section describes the rotor-pendulum system and develops the equations of motion for a static rotor for comparison to pre-existing experimental data. The second section investigates aerodynamic forces acting on the propeller and derives the equations of motion for the full rotor-pendulum system. The third section provides new experimental results for the rotor-pendulum, with a comparison to model predictions. The final section summarizes the paper and ongoing work.

ROTOR DYNAMICS

This paper utilizes a rotor-pendulum to investigate the effect of wind on a small, stiff propeller. The rotor-pendulum is a variation of the gyro-pendulum, which is a spherical pendulum with a rapidly spinning mass on the mobile end that causes the system to precess and nutate. Figure 1 shows the rotor-pendulum system: a gyro-pendulum with the spinning mass replaced by a propeller. Consider inertial frame $\mathcal{I} \triangleq (O, \mathbf{e}_1, \mathbf{e}_2, \mathbf{e}_3)$ and intermediate frame $\mathcal{A} \triangleq (O, \mathbf{a}_1, \mathbf{a}_2, \mathbf{a}_3)$, where $\mathbf{a}_3 = \mathbf{e}_3$ and $\mathbf{a}_1 \cdot \mathbf{e}_1 = \cos\theta$. Spherical frame $\mathcal{B} \triangleq (O, \mathbf{b}_1, \mathbf{b}_2, \mathbf{b}_3)$ satisfies $\mathbf{b}_2 = \mathbf{a}_2$ and $\mathbf{b}_1 \cdot \mathbf{a}_1 = \cos\phi$. The hub frame is $\mathcal{C} \triangleq (O', \mathbf{c}_1, \mathbf{c}_2, \mathbf{c}_3)$, where $\mathbf{c}_3 = \mathbf{b}_3$ and $\mathbf{c}_1 \cdot \mathbf{b}_1 = \cos\psi$. Let N_b represent the number of propeller blades and the superscript $^{(n)}$, where $n = 1, 2$, or 3, denote the blade index, so that frame $\mathcal{D}^{(n)} \triangleq (H^{(n)}, \mathbf{d}_1^{(n)}, \mathbf{d}_2^{(n)}, \mathbf{d}_3^{(n)})$ has origin at the blade hinge, and rotates about $\mathbf{c}_2$ by the flap-angle β. (The blade index $^{(n)}$ is included only where needed for clarity.) Let r denote the displacement along the length of the blade of a point P with respect to O', and dr be the differential position. The differential forces, moments, and mass are denoted $Fdr \triangleq dF$, $Mdr \triangleq dM$, and $mdr \triangleq dm$, where the quantities F, M, and m are each measured per unit length.

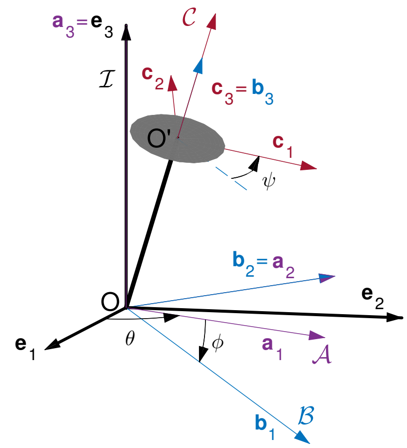

FIGURE 1: REFERENCE FRAMES

The blade-flap angle is derived under the assumption that O' is fixed in inertial space and the blade rotates around the hub in the $\mathbf{c}_3$ direction at a constant rate Ω such that $\Omega t = \psi$, where ψ is the blade azimuth. (The assumption that O' is fixed is relaxed in the analysis of the rotor-pendulum system.) Let $\mathbf{r}_{P/O'}$ denote the position of blade-element P with respect to O'; ${}^{\mathcal{I}}\mathbf{v}_{P/O'} = \frac{{}^{\mathcal{I}}d}{dt}\left(\mathbf{r}_{P/O'}\right)$ and ${}^{\mathcal{I}}\mathbf{a}_{P/O'} = \frac{{}^{\mathcal{I}}d}{dt}\left({}^{\mathcal{I}}\mathbf{v}_{P/O'}\right)$ denote the inertial kinematics. Figure 2 denotes the hinge offset $e = \|\mathbf{r}_{H/O'}\|$; $R - e = \|\mathbf{r}_{Q/H}\|$ is the length of the portion of the blade beyond the hinge offset and $r - e = \|\mathbf{r}_{P/H}\|$ is the distance from the hinge offset to point P. Let $S_\beta = \sin\beta$ and $C_\beta = \cos\beta$. Using the cross product with the angular velocity ${}^{\mathcal{I}}\omega^{\mathcal{C}} = \Omega\mathbf{c}_3$ (${}^{\mathcal{I}}\omega^{\mathcal{C}} = \dot{\theta}\mathbf{a}_3 + \dot{\phi}\mathbf{b}_2 + \Omega\mathbf{c}_3$ where $\dot{\theta} = \dot{\phi} = 0$ due to the fixed hub) to differentiate the unit vectors $\mathbf{c}_1$ and $\mathbf{c}_2$, the inertial kinematics are

$$\mathbf{r}_{P/O'} = (e + (r-e)C_\beta)\mathbf{c}_1 + (r-e)S_\beta\mathbf{c}_3 \tag{1}$$

$$\begin{aligned} {}^{\mathcal{I}}\mathbf{v}_{P/O'} =& -(r-e)\dot{\beta}S_\beta\mathbf{c}_1 \\ &+ (e + (r-e)C_\beta)\Omega\mathbf{c}_2 + (r-e)\dot{\beta}C_\beta\mathbf{c}_3 \end{aligned} \tag{2}$$

$$\begin{aligned} {}^{\mathcal{I}}\mathbf{a}_{P/O'} =& [-(r-e)(\ddot{\beta}S_\beta + \dot{\beta}^2C_\beta) - (e + (r-e)C_\beta)\Omega^2]\mathbf{c}_1 \\ & -2(r-e)\dot{\beta}\Omega S_\beta\mathbf{c}_2 + [(r-e)\ddot{\beta}C_\beta - (r-e)\dot{\beta}^2S_\beta]\mathbf{c}_3. \end{aligned} \tag{3}$$

Figure 2 shows the differential forces on the blade element at P: dF_1 is the tension force; dF_2 is the sum of the lift and drag components in the $\mathbf{c}_1$–$\mathbf{c}_2$ plane; dF_3 is the sum of the lift and drag components in the $\mathbf{c}_1$–$\mathbf{c}_3$ plane; and gdm is the weight. The total differential force acting on a blade element is

$$\begin{aligned} \mathbf{dF}_P^{(n)} =& \left(-dF_1C_\beta - dF_3S_\beta\right)\mathbf{c}_1 + \left(-dF_2\right)\mathbf{c}_2 \\ &+ \left(-dF_1S_\beta + dF_3C_\beta - gdm\right)\mathbf{c}_3. \end{aligned} \tag{4}$$

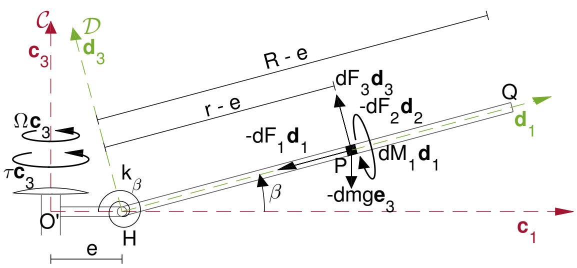

FIGURE 2: FREE-BODY DIAGRAM

Equating the mass times the acceleration (Eqn. (3)) with the force (Eqn. (4)) in the $\mathbf{c}_3$ direction according to Newton's second law yields the differential tension force dF_1, which is used in the angular-momentum form of Newton's second law. The angular momentum of the point P with respect to O' is ${}^{\mathcal{I}}\mathbf{h}_{P/O'} = \mathbf{r}_{P/O'} \times (dm^{\mathcal{I}}\mathbf{v}_{P/O'})$, i.e.,

$$\begin{aligned}{}^{\mathcal{I}}\mathbf{h}_{P/O'} = \; & dm[-(r-e)eS_\beta\Omega - \frac{1}{2}(r-e)^2 S_{2\beta}\Omega]\mathbf{c}_1 \\ & + dm[-(r-e)^2\dot{\beta} - (r-e)eC_\beta\dot{\beta}]\mathbf{c}_2 \\ & + dm[(e+(r-e)C_\beta)^2\Omega]\mathbf{c}_3.\end{aligned} \tag{5}$$

Blade-Flapping Equations Of Motion

The above equations are now used to derive the blade-flapping equations for a rotor with a fixed hub, using the angular-momentum form of Newton's second law. The $\mathbf{c}_2$ component of the inertial derivative of the angular momentum is

$$\begin{aligned}\frac{{}^{\mathcal{I}}d}{dt}\left({}^{\mathcal{I}}\mathbf{h}_{P/O'}\right)\cdot\mathbf{c}_2 = & dm[(-(r-e)^2-(r-e)eC_\beta)\ddot{\beta} \\ & +(r-e)eS_\beta\dot{\beta}^2 + (-(r-e)eS_\beta - \frac{1}{2}(r-e)^2 S_{2\beta})\Omega^2]\end{aligned} \tag{6}$$

and the corresponding moment $\mathbf{M}_{O'}\cdot\mathbf{c}_2$ is

$$\begin{aligned}\mathbf{c}_2\cdot\int_0^R \mathbf{r}_{P/O'}\times\mathbf{dF}_P^{(n)} = & -\int_e^R (eC_\beta + (r-e))dF_3 \\ & + \int_e^R eS_\beta dF_1 + \int_e^R (e+(r-e)C_\beta)gdm + k_\beta\beta,\end{aligned} \tag{7}$$

where the final term is the torsional spring moment.

The following substitutions are made according to convention [17]: I_β is the blade moment of inertia, N_β is the blade static moment, M'_β is the aerodynamic moment on the blade, and ω_{β_0} is the torsional spring natural frequency, i.e., $I_\beta = \int_e^R (r-e)^2 dm$, $N_\beta = \int_e^R (r-e)dm$, $M'_\beta = \int_e^R (r-e)dF_3$, and $\omega_{\beta_0} = \sqrt{k_\beta/I_\beta}$. The flap angle β is expected to remain sufficiently small to permit the small-angle assumption [9, 12]. Set $\nu_\beta^2 = (1 + N_\beta e/I_\beta + \omega_{\beta_0}^2/\Omega^2)$, and define ρ as the density of air, C_{ℓ_α} as the lift slope, c as the blade chord, and consider the Lock number $\gamma = \rho C_{\ell_\alpha} cR^4/I_\beta$. We have $M'_\beta/(I_\beta\Omega^2) = \gamma M_\beta$, where $M_\beta = (\rho C_{\ell_\alpha} cR^4\Omega^2)^{-1}\int_e^R (r-e)dF_3$. Setting Eqn. (6) equal to Eqn. (7) yields the canonical blade-flapping equation (intermediate steps omitted for length), i.e.,

$$\overset{**}{\beta} + \nu_\beta^2\beta = \gamma M_\beta - \frac{gN_\beta}{\Omega^2 I_\beta}, \tag{8}$$

where * denotes differentiation with respect to ψ, following convention [9].

The following parameters arise in the solution to M_β: θ_0 is the blade pitch at the hinge, θ_{tw} is the linear blade twist, and $\lambda_i = \lambda_0(1 + k_x r\cos\psi)$ is the inflow ratio using a linear inflow model [9]. When investigating blade flapping, uniform inflow is often assumed [9, 10, 12, 15]; however, Niemiec and Gandhi [18] showed that using uniform inflow in trim calculations considerably underpredicts pitching moment as compared to linear inflow, so we use a linear inflow model here. The average inflow ratio λ_0 is calculated implicitly, however a fixed value shows sufficient agreement with the implicit calculation over a range of conditions. The parameter $k_x = (15\pi/23)\tan(\chi/2)$ is taken from the model by Pitt and Peters [9], where $\chi = \tan^{-1}(\mu/\lambda_0)$ [19], and μ is the advance ratio of the propeller, which is the ratio of wind speed over the hub to the tip speed of the blades. After solving for M_β in order to identify the steady-state blade-flapping response (omitted due to length constraint) and defining $e' \triangleq e/R$, Eqn. (8) becomes

$$\begin{aligned}& \overset{**}{\beta} + \frac{\gamma}{8}\left[1 - \frac{8e'}{3} + \left(\frac{4}{3} - 4e'\right)\mu S_\psi\right]\overset{*}{\beta} \\ & + \left\{\frac{\gamma}{8}\left[\left(\frac{4}{3} - 2e'\right)\mu C_\psi + (1-2e')\mu^2 S_{2\psi}\right] + \nu_\beta^2\right\}\beta \\ & = \frac{\gamma}{8}\theta_0\left[1 - \frac{4e'}{3} + \left(\frac{8}{3} - 4e'\right)\mu S_\psi + (2-4e')\mu^2 S_\psi^2\right] \\ & + \frac{\gamma}{8}\theta_{tw}\left[\frac{4}{5} - e' + \left(2 - \frac{8e'}{3}\right)\mu S_\psi + \left(\frac{4}{3} - 2e'\right)\mu^2 S_\psi^2\right] \\ & - \frac{\gamma}{8}\lambda_0\left[\frac{4}{3} - 2e' + (2-4e')\mu S_\psi\right] \\ & - \frac{\gamma}{8}\lambda_0 k_x\left[\left(1 - \frac{4e'}{3}\right)C_\psi + \left(\frac{2}{3} - e'\right)\mu S_{2\psi}\right] - \frac{gN_\beta}{\Omega^2 I_\beta},\end{aligned} \tag{9}$$

where the forcing terms on the right side and the $\overset{*}{\beta}$ term result from the solution to M_β, and the second- and higher-order e' terms are not shown due to space limitations.

Although we are primarily interested in the propeller's behavior in wind, setting the advance ratio μ to zero (as in hover) allows us to represent the propeller as a damped second-order system in order to gain intuition about the system. Here the forcing function arises from a (virtual) periodic increase in angle of attack analogous to a full-size helicopter's cyclic pitch input, e.g., the angle of attack is higher on the advancing side, lower on the retreating side, and unchanged over the nose and tail. As we are unable to physically change the angle of attack of each blade on the small propeller, the solution serves only as a theoretical tool for comparison against full-size helicopters. Redefining Eqn. (9) using the normalized derivative with respect to time, i.e., $\overset{*}{\beta} \triangleq \dot{\beta}/\Omega$ and setting $\mu = 0$ yields the aforementioned classical, damped second-order system with natural frequency ω_n, damping ratio ζ, and forcing function $A\Omega^2 \sin(\Omega t)$, where A is a constant, i.e.,

$$\ddot{\beta} + 2\zeta\omega_n\dot{\beta} + \omega_n^2\beta = A\Omega^2\sin(\Omega t). \tag{10}$$

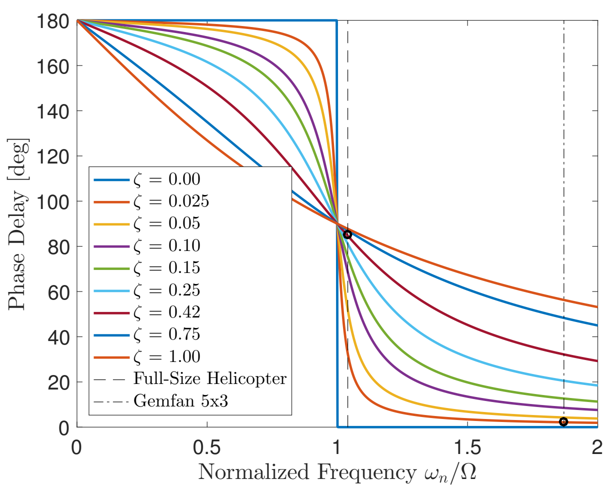

FIGURE 3: BLADE-FLAPPING PHASE DELAY IN HOVER (ADAPTED FROM [17])

Comparing Eqn. (10) to Eqn. (9), the damping ratio is $\zeta = \gamma/(16\nu_\beta)\left(1 - 8e'/3 + 2e'^2 - e'^4/3\right)$ and the natural frequency is $\omega_n = \Omega\nu_\beta$. Solving Eqn. (10) yields the particular solution

$$\beta_p = \beta_{max}\sin(\Omega t - \phi_D), \tag{11}$$

where

$$\begin{aligned} \beta_{max} &= \frac{A}{\sqrt{\left(\left(\frac{\omega_n}{\Omega}\right)^2 - 1\right)^2 + \left(2\zeta\frac{\omega_n}{\Omega}\right)^2}}, \\ \phi_D &= \tan^{-1}\left(\frac{2\zeta\frac{\omega_n}{\Omega}}{\left(\frac{\omega_n}{\Omega}\right)^2 - 1}\right). \end{aligned} \tag{12}$$

Here, β_{max} indicates the maximum flapping amplitude variation of the propeller, and ϕ_D represents the angular delay between the maximum aerodynamic force and the maximum flapping amplitude.

Figure 3 shows phase-delay solutions to Eqn. (10) for varying natural frequency and damping ratio. For a typical full-size helicopter with $\nu_\beta = 1.04$ and $\zeta = 0.42$, the phase delay is 85° [17]. Analysis of a small, stiff propeller is performed using a Gemfan 5030 propeller rotating at 8000 rpm. The propeller is 2.7 grams and 12.7 centimeters in diameter, with a 1.5 centimeter chord. Assuming $e' = 0.1$ and $k_\beta = 3$ Nm/rad based on model and experimental fit below, the values of the characteristic blade-parameters are as follows: scaled natural frequency $\nu_\beta = 1.9$, damping ratio $\zeta = 0.026$, and Lock number $\gamma = 1.04$. Due to the atypical values of these parameters compared to full-scale helicopters, the hover flap response is also atypical; the phase delay is $\phi_D = 2.2°$ as shown by Fig. 3, with amplitude $\beta_{max} = 0.053°$.

When solving Eqn. (9) assuming wind over the hub such that $\mu \neq 0$, periodic terms do not allow for a true analytical solution. However, if we take the Fourier series solution and assume first harmonics only, i.e., $\beta(\psi) = \beta_0 + \beta_{1c}\cos\psi + \beta_{1s}\sin\psi$, we can harmonically match constant and periodic (sine and cosine) terms on each side of the equation to achieve an approximate solution [9], which (again omitting higher orders of e') yields

$$\begin{aligned} \beta_0 = \frac{\gamma}{8\nu_\beta^2}\Bigg\{ &-e'\mu\beta_{1c} + \theta_0\left[1 - \frac{4e'}{3} + (1-2e')\mu^2\right] \\ &+\theta_{tw}\left[\frac{4}{5} - e' + \left(\frac{2}{3} - e'\right)\mu^2\right] - \lambda_0\left(\frac{4}{3} - 2e'\right)\Bigg\}, \end{aligned} \tag{13}$$

$$\begin{aligned} \beta_{1c} = \frac{\gamma}{8\left(\nu_\beta^2 - 1\right)}\Bigg\{ &-\left(\frac{4}{3} - 2e'\right)\mu\beta_0 \\ &-\left[1 - \frac{8e'}{3} + \left(\frac{1}{2} - e'\right)\mu^2\right]\beta_{1s} - \lambda_0 k_x\left(1 - \frac{4e'}{3}\right)\Bigg\}, \end{aligned} \tag{14}$$

$$\begin{aligned} \beta_{1s} = \frac{\gamma}{8\left(\nu_\beta^2 - 1\right)}\Bigg\{ &\left[1 - \frac{8e'}{3} - \left(\frac{1}{2} - e'\right)\mu^2\right]\beta_{1c} \\ &+\theta_0\left(\frac{8}{3} - 4e'\right)\mu + \theta_{tw}\left(2 - \frac{8e'}{3}\right)\mu - \lambda_0(2 - 4e')\mu\Bigg\}. \end{aligned} \tag{15}$$

Equations (13–15) yield very different characteristics compared to Eqn. (12), primarily due to the presence of the linear inflow term $\lambda_0 k_x$ in Eqn. (14), which changes the azimuth an-

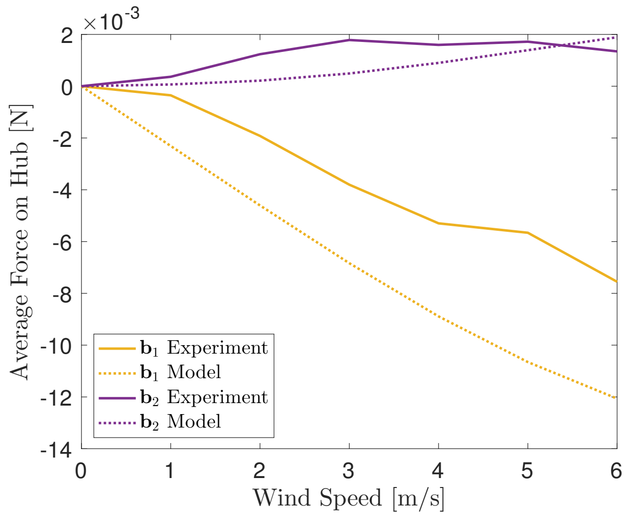

FIGURE 4: HUB FORCE IN WIND

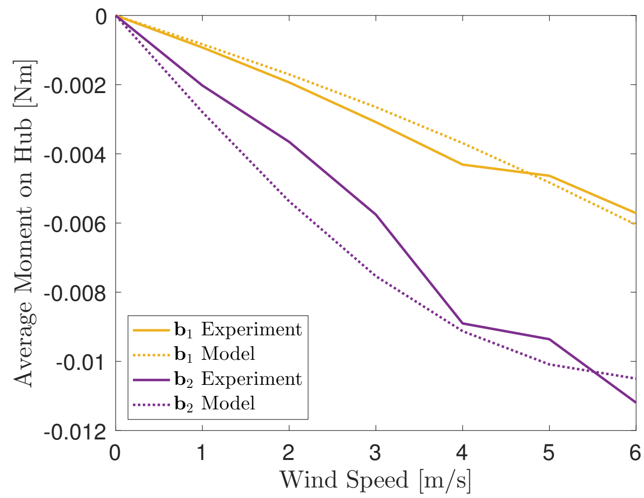

FIGURE 5: HUB MOMENT IN WIND

gle of the maximum aerodynamic force. Specifically, the linear inflow model yields a 97% change in phase delay compared to Eqn. (12), versus assuming uniform inflow in Eqns. (13–15), which yields just a one percent change in phase delay compared to Eqn. (12). In order to identify β_{max} and ϕ_D with $\mu \neq 0$, we apply the sinusoidal relationship $A\cos(\omega t + \phi) = I\cos\omega t - Q\sin\omega t$ [20], which shows

$$\beta(\psi) = \beta_0 + \sqrt{\beta_{1c}^2 + \beta_{1s}^2}\sin\left[\psi - \left(\tan^{-1}\left(\frac{\beta_{1s}}{\beta_{1c}}\right) - \frac{\pi}{2}\right)\right]. \quad (16)$$

Comparing Eqn. (16) to Eqn. (11) indicates the maximum flap amplitude variation $\beta_{max} = \sqrt{\beta_{1c}^2 + \beta_{1s}^2}$ and phase delay $\phi_D = \tan^{-1}(\beta_{1s}/\beta_{1c}) - \pi/2$. Assuming the same values as above for e', k_β, and propeller speed, the phase delay and maximum flap of the propeller in 3 m/s wind are $\phi_D = 81°$ and $\beta_{max} = 0.10°$. Using force and moment calculations from the next section, the blade-flapping model is used to compare forces and moments on a fixed hub to those taken in a prior experiment using an ATI Nano 17 six-axis Force-Torque transducer, with flow speed measurements provided by a Thomas Scientific Traceable hotwire anemometer. In order to best fit the model to the experiment, values for e' and k_β are chosen as $e' = 0.1$ and $k_\beta = 3$ Nm/rad, yielding the results in Figs. 4 and 5, which show agreement between model and experiment in the magnitude and direction of forces at a propeller speed of 8000 rpm over a range of wind speeds.

ROTOR-PENDULUM DYNAMICS

Figure 6 introduces two additional reference frames in order to describe the aerodynamic forces, which depend on the magnitude and direction of the wind as well as the phase delay of the propeller. Let ${}^{\mathcal{I}}\mathbf{V}_\infty$ represent the velocity of the wind in the inertial frame, and ${}^{\mathcal{B}}\mathbf{V}_\infty$ represent the velocity of the wind experienced by an observer at point O' in the spherical frame due to the combination of the wind and the motion of point O'. Define the wind frame $\mathcal{U} \triangleq (O', \mathbf{u}_1, \mathbf{u}_2, \mathbf{u}_3)$, where $\mathbf{u}_3 = \mathbf{b}_3$, and $\mathbf{u}_1$ is the direction of the component of ${}^{\mathcal{B}}\mathbf{V}_\infty$ in the plane perpendicular to $\mathbf{b}_3$. Also consider the phase-delay frame $\mathcal{V} \triangleq (O', \mathbf{v}_1, \mathbf{v}_2, \mathbf{v}_3)$, where $\mathbf{v}_3 = \mathbf{u}_3$ and $\mathbf{v}_1 \cdot \mathbf{u}_1 = \cos\phi_D$. From this definition, $\mathbf{v}_2$ will correspond to the direction of maximum flapping.

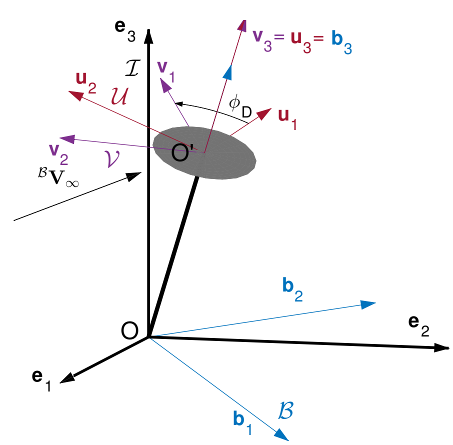

FIGURE 6: ROTOR-PENDULUM $\mathcal{U}$ AND $\mathcal{V}$ FRAMES

The hub forces in the plane perpendicular to $\mathbf{b}_3$, i.e., $\mathbf{F}_{O'}^{\perp} \triangleq \mathbf{F}_{O'} - (\mathbf{F}_{O'} \cdot \mathbf{b}_3)\mathbf{b}_3$, are a combination of the tilt of the thrust vector and the drag forces on the blades. Consider the case of two blades. Starting from Eqn. (4), and averaging the force over an entire revolution, the planar hub force is

$$\mathbf{F}_{O'}^{\perp} = \frac{N_b}{2\pi}\int_0^{2\pi}\left[\int_0^R (-dF_2\mathbf{c}_2\cdot\mathbf{u}_1)\,\mathbf{u}_1 - \int_e^R S_\beta dF_3\mathbf{c}_1\right]d\psi, \quad (17)$$

where $\mathbf{c}_2\cdot\mathbf{u}_1 = -S_\psi$. The differential blade tension forces $dF_1^{(1)}$ and $dF_1^{(2)}$ cancel out because $dF_1^{(1)} = -dF_1^{(2)}$, leaving only the dF_2 and dF_3 components. The dF_3 component is calculated from GemFan 5030 propeller experimental thrust data at a range of speeds; the dF_2 component arises from induced drag.

The dF_3 term in Eqn. (17) is converted from the $\mathcal{C}$ frame to the $\mathcal{V}$ frame, which does not rotate with ψ. According to Eqn. (16), β responds as a once-per-revolution sinusoid $\beta(\psi) = \beta_0 + \beta_{max}S_{(\psi-\phi_D)}$. Making the small-angle assumption based on the calculated magnitude of β_{max}, Eqn. (17) becomes

$$\begin{aligned}\mathbf{F}_{O'}^{\perp} = \frac{N_b}{2\pi}\int_0^{2\pi}&\left[\int_0^R (-dF_2\mathbf{c}_2\cdot\mathbf{u}_1)\,\mathbf{u}_1 - \left(\beta_0+\beta_{max}S_{(\psi-\phi_D)}\right)\right.\\ &\left.\times\int_e^R \left(C_{(\psi-\phi_D)}\mathbf{v}_1 + S_{(\psi-\phi_D)}\mathbf{v}_2\right)dF_3\right]d\psi.\end{aligned} \quad (18)$$

The force along $\mathbf{v}_1$ resulting from dF_3 in Eqn. (18) as well as all forces due to β_0 integrate to zero over one full rotation due to the sinusoidal term, leaving only the $\mathbf{v}_2$ component.

Quadrotors experience high induced drag, which results from the lift force and induced angle of attack. Let $\alpha_{ind} = \arctan(\lambda_i/0.75)$ denote the induced angle of attack (using for simplicity the average angle, rather than integrating across the blade), which results from the velocity of the wind relative to the rotating blade; $\alpha_{eff} = \alpha_{geo} - \alpha_{ind}$ be the effective angle of attack; and α_{geo} be the geometric angle of attack resulting from the blade pitch relative to the $\mathbf{d}_2$ axis. Induced drag is the only non-negligible component of differential force dF_2, thus

$$dF_2 = \frac{1}{2}\rho\left(\Omega r - (\mathbf{c}_2\cdot\mathbf{u}_1)\,({}^{\mathcal{B}}\mathbf{V}_\infty\cdot\mathbf{u}_1)\right)^2 c\,C_{\ell_\alpha}\alpha_{eff}S_{\alpha_{ind}}\,dr. \quad (19)$$

There also exist bluff body drag forces acting in the direction of the wind on the swept area of the rotor and the pendulum rod. The bluff force on each component is

$$\begin{aligned}\mathbf{F}_{R_{bluff}} &= \frac{1}{2}\rho||{}^{\mathcal{B}}\mathbf{V}_\infty||^2\left({}^{\mathcal{B}}\hat{\mathbf{V}}_\infty\cdot\mathbf{b}_3\pi R^2\right)C_D{}^{\mathcal{B}}\hat{\mathbf{V}}_\infty,\\ \mathbf{F}_{\ell_{bluff}} &= \frac{1}{2}\rho||{}^{\mathcal{B}}\mathbf{V}_\infty||^2\left({}^{\mathcal{B}}\hat{\mathbf{V}}_\infty\cdot\mathbf{u}_1 w\ell\right)C_D{}^{\mathcal{B}}\hat{\mathbf{V}}_\infty,\end{aligned} \quad (20)$$

where ${}^{\mathcal{B}}\hat{\mathbf{V}}_\infty = {}^{\mathcal{B}}\mathbf{V}_\infty/||{}^{\mathcal{B}}\mathbf{V}_\infty||$, rod width $w = 1$ cm and the drag coefficient $C_D = 1.28$ [21] is taken by approximating each component as a three-dimensional flat plate.

The moment on the hub in the plane perpendicular to $\mathbf{b}_3$, i.e., $\mathbf{M}_{O'}^{\perp} \triangleq \mathbf{M}_{O'} - (\mathbf{M}_{O'}\cdot\mathbf{b}_3)\mathbf{b}_3$, is derived from the spring, hinge, and the pitching moment of the airfoil. The lift and weight forces do not transmit a moment to the hub due to the nature of the hinge, leading to their absence in the following moment equation as compared to Eqn. (7) above. The moment in the plane perpendicular to $\mathbf{b}_3$ is

$$\begin{aligned}\mathbf{M}_{O'}^{\perp} =& \frac{N_b}{2\pi}\int_0^{2\pi} -\left[k_\beta\beta + eS_\beta\int_e^R dF_1\right]\mathbf{c}_2 d\psi\\ &+\frac{N_b}{2\pi}\int_0^{2\pi}\int_0^R (dM_1\mathbf{c}_1\cdot\mathbf{u}_2)\,\mathbf{u}_2 d\psi,\end{aligned} \quad (21)$$

where $\mathbf{c}_1\cdot\mathbf{u}_2 = S_\psi$.

The first half of Eqn. (21) is converted from the rotating $\mathcal{C}$ frame to the $\mathcal{V}$ frame as in Eqn. (17), which yields

$$\begin{aligned}\mathbf{M}_{O'}^{\perp} =& \frac{N_b}{2\pi}\int_0^{2\pi}\left[\left(k_\beta + e\int_e^R dF_1\right)\right.\\ &\left.\times\left(\beta_0+\beta_{max}S_{(\psi-\phi_D)}\right)\left(S_{(\psi-\phi_D)}\mathbf{v}_1 - C_{(\psi-\phi_D)}\mathbf{v}_2\right)\right]d\psi\\ &+\frac{N_b}{2\pi}\int_0^{2\pi}\int_0^R (dM_1\mathbf{c}_1\cdot\mathbf{u}_2)\,\mathbf{u}_2 d\psi.\end{aligned} \quad (22)$$

The moment along $\mathbf{v}_2$ from the first half of Eqn. (22) and the moment due to β_0 integrate to zero over one full rotation due to the sinusoidal term, leaving only the $\mathbf{v}_1$ component.

The centrifugal or tension differential force $dF_1 = r\Omega^2 dm$ is found by equating the $\mathbf{c}_1$ component in Eqns. (3) and (4), applying small-angle simplifications to trigonometric terms involving β, and assuming that $\dot{\beta}$ and $\ddot{\beta}$ are negligible in comparison to Ω.

The differential moment dM_1 on the hub due to the airfoil pitching is calculated by approximating the shape of the Gemfan 5030 airfoil as a 4-digit NACA airfoil, and using the calculation for this shape to determine the coefficient of blade pitching moment according to [22, pp. 275-278], [23, pp. 113-114]. The blade pitching differential moment is

$$dM_1 = \frac{1}{2}\rho\left(\Omega r - (\mathbf{c}_2\cdot\mathbf{u}_1)\,({}^{\mathcal{B}}\mathbf{V}_\infty\cdot\mathbf{u}_1)\right)^2 c^2 c_{m,c/2}dr, \quad (23)$$

where $c_{m,c/2}$ is the blade pitch moment coefficient per unit span at the half chord.

The forces and moments derived above are applied to the rotor-pendulum in Fig. 7, where $\mathbf{F}_{O'} = \mathbf{F}_{O'}^{\perp} + C_\beta dF_3\mathbf{c}_3$ and $\mathbf{M}_{O'} = \mathbf{M}_{O'}^{\perp} + \tau\mathbf{c}_3$, and τ is the magnitude of the moment produced by motor torque. Figure 7 also shows the force $-(m_M + m_R)g\mathbf{e}_3$ due to the weight of the motor and rotor at the hub, the force $-m_\ell g\mathbf{e}_3$ due to the weight of the rod, and the bluff body forces.

The position of the point O' with respect to O is $\mathbf{r}_{O'/O} = \ell\mathbf{b}_3$ and the corresponding inertial velocity is ${}^{\mathcal{I}}\mathbf{v}_{O'/O} = \ell\dot{\phi}\mathbf{b}_1 + \ell\dot{\theta}S_\phi\mathbf{b}_2$. The angular velocity of frame $\mathcal{B}$ with respect to $\mathcal{I}$ is ${}^{\mathcal{I}}\omega^{\mathcal{B}} = \dot{\theta}\mathbf{a}_3 + \dot{\phi}\mathbf{b}_2 = -\dot{\theta}S_\phi\mathbf{b}_1 + \dot{\phi}\mathbf{b}_2 + \dot{\theta}C_\phi\mathbf{b}_3$, and the angular velocity of the rotor is ${}^{\mathcal{I}}\omega^{\mathcal{C}} = {}^{\mathcal{I}}\omega^{\mathcal{B}} + \Omega\mathbf{b}_3$. Let ℓ be the length of the rod, m_M and m_R be the mass of the motor and rotor, respectively, and I_ℓ and I_R the moment of inertia matrices for the rod and rotor, respectively. The total angular momentum of the system with respect to origin O is

$$\begin{aligned}{}^{\mathcal{I}}\mathbf{h}_O =& I_\ell{}^{\mathcal{I}}\omega^{\mathcal{B}} + \mathbf{r}_{\ell/O} \times m_\ell{}^{\mathcal{I}}\mathbf{v}_{\ell/O} \\ &+ I_R{}^{\mathcal{I}}\omega^{\mathcal{C}} + \mathbf{r}_{O'/O} \times (m_M + m_R){}^{\mathcal{I}}\mathbf{v}_{O'/O}\end{aligned} \tag{24}$$

and the moment about O is

$$\begin{aligned}\mathbf{M}_O =& \mathbf{M}_{O'} + \frac{\ell}{2}\mathbf{b}_3 \times \left(-m_\ell g\mathbf{e}_3 + \mathbf{F}_{\ell_{bluff}}\right) \\ &+ \ell\mathbf{b}_3 \times \left(-(m_M + m_R)g\mathbf{e}_3 + \mathbf{F}_{O'} + \mathbf{F}_{R_{bluff}}\right).\end{aligned} \tag{25}$$

Assuming that the angular velocity of the rotor Ω is sufficiently large such that the angular velocity ${}^{\mathcal{I}}\omega^{\mathcal{B}}$ may be ignored in the calculation of ${}^{\mathcal{I}}\omega^{\mathcal{C}}$, and defining $m_{O'} \triangleq m_M + m_R$, the equations of motion for the system resulting from Euler's second law are

$$\begin{aligned}\ddot{\theta} = \frac{1}{\left(\frac{m_\ell}{3} + m_{O'}\right)\ell^2 S_\phi}\Big[&-\mathbf{M}_O \cdot \mathbf{b}_1 + \frac{m_R}{3}R^2\dot{\phi}\left(\dot{\theta}C_\phi + \Omega\right) \\ &-2\left(m_{O'} + \frac{m_\ell}{3}\right)\ell^2\dot{\phi}\dot{\theta}C_\phi\Big] - \zeta_{RP}\dot{\theta},\end{aligned} \tag{26}$$

$$\begin{aligned}\ddot{\phi} = \frac{1}{\left(\frac{m_\ell}{3} + m_{O'}\right)\ell^2}\Big[&\mathbf{M}_O \cdot \mathbf{b}_2 + \left(m_{O'} + \frac{m_\ell}{3}\right)\ell^2\dot{\theta}^2 S_\phi C_\phi \\ &+ \left(m_{O'} + \frac{m_\ell}{2}\right)g\ell S_\phi - \frac{m_R}{3}R^2\dot{\theta}S_\phi\left(\dot{\theta}C_\phi + \Omega\right)\Big] - \zeta_{RP}\dot{\phi},\end{aligned} \tag{27}$$

which includes rotor-pendulum damping term ζ_{RP}, representing the natural damping of the bearings, wires, and others components of the physical system. When aerodynamic forces and rotor-pendulum damping are ignored, Eqns. (26) and (27) reduce to the standard gyro-pendulum equations [24, pp. 469-471].

In order to simulate the forces and moments in MATLAB, the wind vector is used to identify $\mu = ||{}^{\mathcal{B}}\mathbf{V}_\infty||/(\Omega R)$, β, and the $\mathcal{U}$ and $\mathcal{V}$ frames, which are used with the above calculations to produce $\mathbf{M}_O$.

Equilibrium analysis is performed by setting $[\dot{\theta}, \ddot{\theta}, \dot{\phi}, \ddot{\phi}]^T = 0$ in Eqns. (26) and (27), assuming small angles such that the norm of the wind velocity in the plane of the rotor is constant, and assuming the parameters listed in Tab. 1. In the case with ${}^{\mathcal{I}}\mathbf{V}_\infty = 0$ m/s, $[\theta_{eq}, \phi_{eq}] = [0°, 180°]$, whereas ${}^{\mathcal{I}}\mathbf{V}_\infty = -3\mathbf{e}_1$ m/s yields $[\theta_{eq}, \phi_{eq}] = [15°, 186°]$. Using state vector $[\theta, \dot{\theta}, \phi, \dot{\phi}]^T$ and solving numerically for the Jacobian matrix, the linearized equations of motion are

$$\frac{d}{dt}\begin{bmatrix}\theta \\ \dot{\theta} \\ \phi \\ \dot{\phi}\end{bmatrix} = \begin{bmatrix}0 & 1 & 0 & 0 \\ -45.6 & -1.39 & -3.99 & -14.6 \\ 0 & 0 & 0 & 1 \\ -0.0306 & 0.150 & -44.1 & -0.991\end{bmatrix}\begin{bmatrix}\theta \\ \dot{\theta} \\ \phi \\ \dot{\phi}\end{bmatrix}, \tag{28}$$

with ${}^{\mathcal{I}}\mathbf{V}_\infty = -3\mathbf{e}_1$ m/s and $\Omega = 8000$ rpm. The eigenvalues of this system are $(-0.528 + 5.98i, -0.528 - 5.98i, -0.664 + 7.45i, -0.664 - 7.45i)$, showing exponential stability with moderate oscillation, which is consistent with simulation. The matrix values differ when varying wind speed with constant Ω, however, the eigenvalues remain in similar locations. Thus the rotor-pendulum without wind settles to the downward vertical, whereas the rotor-pendulum with wind converges to an off-vertical angle approximately 15° from the wind direction.

The rotor-pendulum is simulated using Eqns. (26) and (27) in the presence of a step wind input. Figure 8 shows the simulated trajectory of the tip of the rotor-pendulum projected on the horizontal plane, from the perspective of looking down at the hanging pendulum. As expected, with no wind at all, the rotor-pendulum hangs downward. As the magnitude of the gust

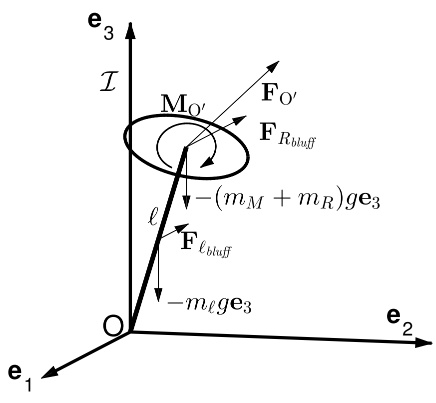

FIGURE 7: ROTOR-PENDULUM FREE-BODY DIAGRAM

Parameter	Name	Value	Units
m_R	rotor mass	0.0027	kg
m_M	motor mass	0.018	kg
m_ℓ	rod mass	0.043	kg
R	rotor radius	0.0635	m
c	chord length	0.015	m
N_b	number of blades	2	[ ]
e	effective hinge offset	0.1	[ ]
k_β	hinge spring const.	3	Nm/rad
I_β	blade inertia	1.81×10^{-6}	kgm^2
ρ	density of air	1.225	kg/m^3
C_{l_α}	airfoil lift slope	2π	[ ]
γ	Lock number	1.04	[ ]
λ_0	avg. inflow ratio	0.075	[ ]
θ_0	root angle of attack	16	deg
θ_{tw}	blade twist	-6.6	deg
ω_{β_0}	spring nat. freq.	1290	rad/s
ν_β	blade scaled nat. freq.	1.9	[ ]
ζ	blade damping coef.	0.026	[ ]
ζ_{RP}	pendulum damp. coef.	1	[ ]

TABLE 1: MODEL PARAMETERS

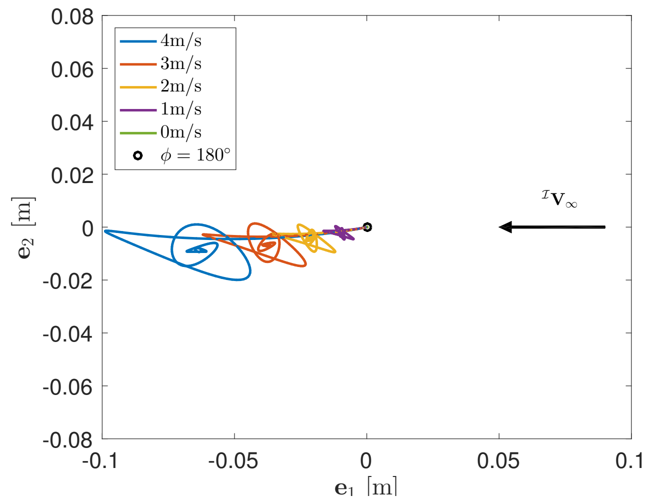

FIGURE 8: SIMULATED ROTOR-PENDULUM

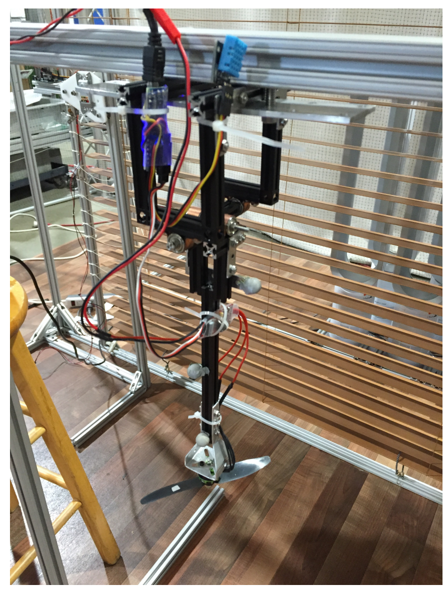

FIGURE 9: ROTOR-PENDULUM STAND

increases, the vertical offset angle and magnitude of oscillation increase, with the rotor-pendulum settling over time to the equilibrium value in the center of the oscillation. As the wind increases, the angle θ about the $\mathbf{e}_3$ axis reduces slightly due to the bluff body force, more closely aligning the pendulum to the wind direction.

EXPERIMENT

In order to validate the rotor-pendulum model, an experimental stand (Fig. 9) was built and tested in a known wind field produced by a set of blower-style Dyson fans (Fig. 10), with the system response identified using 18 OptiTrack motion-capture cameras. The rotor-pendulum test stand was initiated in the downward position.

Tests were performed with a rotor speed of 8000 rpm and wind velocities of 0 m/s and $-3\mathbf{e}_1$ m/s. In order to verify the aerodynamic effects on the rotor, a disk with equal moment of inertia was constructed using a 3D printer and also tested at both wind speeds to investigate possible confounding variables. As expected, when testing without wind, both the rotor and disk exhibit stable equilibria at $\phi = 180°$ and arbitrary θ. Under a constant $-3\mathbf{e}_1$ m/s wind, the stable equilibrium point for the experimental stand with the rotor is $[\theta_{eq}, \phi_{eq}] = [20°, 190°]$, and with the disk is $[\theta_{eq}, \phi_{eq}] = [6°, 182°]$. This result indicates that even in the case of the disk without lifting surfaces, the bluff body aerodynamic drag of the system causes a change in the equilibrium

FIGURE 10: ROTOR-PENDULUM TEST FACILITY

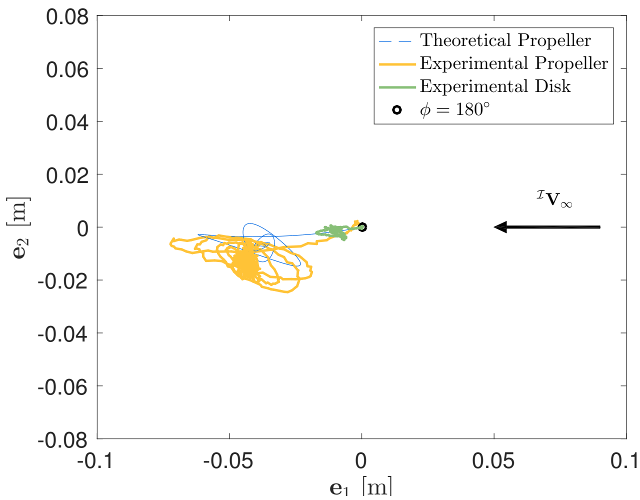

FIGURE 11: ROTOR-PENDULUM EXPERIMENT

point.

A step input for wind from 0 to $-3\mathbf{e}_1$ m/s was generated by quickly changing the angle of the blinds between the fans and the test stand in Fig. 10 in order to maintain a smooth wind flow (as opposed to suddenly opening the blinds). Figure 11 shows the result of this test, as well as a comparison to theoretical results under the same conditions. Without the lifting surfaces of a rotor, bluff body drag moves the disk only slightly, and in the direction approximately parallel to the wind direction as expected. The propeller also moves primarily in the direction of the wind, but at a much greater offset angle ϕ, and progresses in a spiral pattern as it reaches its equilibrium point. This result shows the influence of the lifting surfaces of the propeller, creating a higher moment that also yields slight movement in the $-\mathbf{e}_2$ direction. Theoretical and experimental results show strong agreement, indicating the importance of linear inflow calculations in blade flapping analysis, which dramatically change the flap characteristics compared to hover. Slight inaccuracy between the model and experiment is most likely due to the aerodynamic complexity of the system.

CONCLUSION

This paper presents a dynamic model of a rotor-pendulum based on the aerodynamic response of a small, stiff propeller in wind. The model includes the blade-flapping response of the propeller and the resulting forces and moments. When simplified, the equations-of-motion reduce to those of a gyro-pendulum. State matrices and equilibrium points for the system under particular conditions are numerically identified, showing a stable system with moderate oscillation in the presence of wind. Experimental results show strong agreement with theoretical predictions. Ongoing work includes analysis of the contributions of each of the forces and moments on the system in order to create a tractable model that can be implemented in real time for control. Ongoing work resulting from this paper includes the development of a controllable quadrotor test stand that leverages the blade-flapping response, forces, and moments here to yield feedback controllers capable of stabilizing the quadrotor in response to a gust.

ACKNOWLEDGEMENT

This work was supported by the University of Maryland Vertical Lift Rotorcraft Center of Excellence Army Grant No. W911W61120012. The authors would like to thank Dan Escobar and Elena Shrestha for providing parts and machining, as well as Bharath Govindarajan and Andrew Lind for their blade-flapping and aerodynamics expertise.

REFERENCES

[1] Rabbath, C., and Lechevin, N., 2010. *Safety and Reliability in Cooperating Unmanned Aerial Systems*. World Scientific Publishing Co., Singapore, Chapter 1.

[2] Atkins, E. M., 2010. "Risk identification and management for safe UAS operation". In Int. Symp. on Systems and Control in Aeronautics and Astronautics, Harbin, China, pp. 774–779.

[3] Zarovy, S., Costello, M., and Mehta, A., 2012. "Experimental method for studying gust effects on micro rotorcraft". *Proceedings of the Institution of Mechanical Engineers*, ***227***(4), mar, pp. 703–713.

[4] Lu, H., Liu, C., Guo, L., and Chen, W.-H., 2015. "Flight

control design for small-scale helicopter using disturbance-observer-based backstepping". *Journal of Guidance, Control, and Dynamics,* ***38***(11), pp. 2235–2240.

[5] García Carrillo, L. R., Dzul López, A. E., Lozano, R., and Pégard, C., 2013. *Quad rotorcraft control vision-based hovering and navigation*. Springer, London, England, Chapter 2.

[6] Liu, H., Bai, Y., Lu, G., Shi, Z., and Zhong, Y., 2013. "Robust tracking control of a quadrotor helicopter". *Journal of Intelligent & Robotic Systems,* ***75***(3-4), may, pp. 595–608.

[7] Mellinger, D., and Kumar, V., 2011. "Minimum snap trajectory generation and control for quadrotors". In Proc. IEEE Int. Conf. Robotics and Automation, Shanghai, China, pp. 2520–2525.

[8] Lupashin, S., Schöllig, A., Sherback, M., and D'Andrea, R., 2010. "A simple learning strategy for high-speed quadrocopter multi-flips". In Proc. IEEE Int. Conf. Robotics and Automation, Anchorage, AK, pp. 1642–1648.

[9] Leishman, J. G., 2006. *Principles of Helicopter Aerodynamics*, 2nd ed. Cambridge University Press, New York, NY, Chapter 2,3,4.

[10] Mahony, R., Kumar, V., and Corke, P., 2012. "Modeling, estimation, and control of quadrotor". *IEEE Robotics and Automation Magazine*, sep, pp. 20–32.

[11] Bangura, M., and Mahony, R., 2012. "Nonlinear dynamic modeling for high performance control of a quadrotor". In Proc. Australasian Conf. Robotics and Automation, Wellington, New Zealand, pp. 1–10.

[12] Hoffmann, G., Huang, H., Waslander, S., and Tomlin, C., 2007. "Quadrotor helicopter flight dynamics and control: theory and experiment". In Proc. AIAA Guidance, Navigation, and Control Conf., Paper AIAA 2007-6461, Hilton Head, SC.

[13] Sydney, N., Smyth, B., and Paley, D., 2013. "Dynamic control of autonomous quadrotor flight in an estimated wind field". In Proc. IEEE Conf. Decision and Control, Firenze, Italy, pp. 3609–3616.

[14] Bristeau, P. J., Martin, P., Salaün, E., and Petit, N., 2009. "The role of propeller aerodynamics in the model of a quadrotor UAV". In Proc. European Control Conference, Budapest, Hungary, pp. 683–688.

[15] Pounds, P., Mahony, R., and Corke, P., 2010. "Modelling and control of a large quadrotor robot". *Control Engineering Practice,* ***18***(7), pp. 691–699.

[16] Yeo, D., Sydney, N., and Paley, D. A., 2016. "Onboard flow sensing for rotary-wing UAV pitch control in wind". In Proc. AIAA Guidance Navigation and Control Conf., Paper AIAA 2016-1386, San Diego, CA.

[17] Prouty, R., 2005. *Helicopter Performance, Stability, and Control*. Krieger Publishing Company, Malabar, FL, Chapter 7.

[18] Niemiec, R., and Gandhi, F., 2016. "Effects of inflow model on simulated aeromechanics of a quadrotor helicopter". In AHS International 72nd Annual Forum, West Palm Beach, FL, pp. 1–13.

[19] Chen, R., 1989. A survey of nonuniform inflow models for rotorcraft flight dynamics and control applications. Tech. rep., NASA, Moffett Field, CA.

[20] Anderson, J. B., 2005. *Carrier transmission*. IEEE Press, Piscataway, NJ, Chapter 3.

[21] Hall, N., 2015. Shape Effects on Drag. On the WWW, June. URL http://www.grc.nasa.gov/WWW/k-12/airplane/shaped.html.

[22] Anderson, J. D., 1991. *Fundamentals of Aerodynamics*. McGraw-Hill, New York, NY, Chapter 4.

[23] Abbot, I., and Doenhoff, A., 1959. *Theory of Wing Sections*. Dover Publications, New York, NY, Chapter 6.

[24] Kasdin, N. J., and Paley, D. A., 2011. *Engineering Dynamics: A Comprehensive Introduction*. Princeton University Press, Princeton, NJ, Chapter 11.